Inspection of Surface Strain in Materials using Optical Flow

Katharine Chivers and William Clocksin
Department of Materials Science, and Computer Laboratory
University of Cambridge
Cambridge CB2 3QG, UK
wfc@CL.cam.ac.uk

Abstract

We have developed optical flow based techniques for finding the surface strain of an untreated sample of material from a sequence of images taken during the application of force from a test rig. Not all optical flow algorithms have suitable functional characteristics for this task, as image sequences are characterised by both short- and long-range displacements, non-rigid deformations, as well as a low signal-to-noise ratio and methodological artefacts. We show how optical flow can be used as a high confidence estimator of the strain tensor characterising the deformation of the material. We give results from three studies: Aluminium alloy under axial tension, the formation of kink bands in compressed carbon-fibre composite, and non-homogeneous strain fields in welded alloy. These studies have demonstrated the capabilities of a new optical flow algorithm. Because the algorithm offers increased accuracy near motion contrast boundaries, its application has resulted in new observations of interest to materials scientists.

1 Introduction

The measurement of strain is of vital importance in the investigation of the mechanical properties of materials. Strain is the local spatial gradient of the displacements that occur within a material when it is placed under stress. Its value depends on the scale at which it is measured. At a sufficiently macroscopic scale the strain will be homogeneous (for a suitable geometry) and have a single value. At smaller scales the strain field is not homogeneous, and will be affected by pores, cracks, impurities and other defects of the material.

Traditionally strain has been measured by resistance strain gauges [10] or the measurement of distance between set points, both of which give single values without indication of whether they are averages of homogeneous or inhomogeneous strain. Interferometric techniques [3, 15] give better resolution and multiple values over an area but they tend to be much more limited in the range of strain that they can measure.

Image processing has an obvious use, as the same analysis process can be used for images taken at different magnifications and hence different resolutions. Optical flow

BMVC 2000 doi:10.5244/C.14.41

algorithms are well known in the field of image processing (see reviews [1, 2]), but they have found only very limited application to strain measurement for in-situ mechanical testing. In materials science, most attempts at using digital image correlation for the measurement of displacement, and hence the determination of strain, have painted the surface with black-and-white speckles [11] or a reflective powder [16] in order to increase contrast. This gives more texture to aid the image processing, but can obscure the metallographic detail. Furthermore, because long-range displacements (of more than say 8 pixels) are common in strain experiments, correlation-based methods have been favoured over gradient-based methods [6]. Yet, the non-rigid deformations inherent in strain flow are not ideal for correlation-based approaches. Chivers [4] carried out a study of the performance of various optical flow algorithms applied to strain measurement problem on metal alloys, and found that the method by Clocksin [7] gave the best performance. This method computes, at each point where a flow vector is required, a multi-modal probability distribution function to estimate the maximum likelihood of a displacement. Both short-and long-range displacements can be found, as well as the displacements that form non-rigid deformations. The method is particularly accurate at motion contrast borders, an essential property for strain measurements.

Simoncelli et al. [13] also discuss probability distributions of optical flow, but they model a distribution function as a single gaussian. Such a distribution does not represent multimodal distributions and therefore does not offer the benefits conferred by the method of Clocksin [7]. Registration algorithms designed for non-rigid deformations have been reviewed by Hayton et al. [8], who also introduce a new one. It is possible that such registration algorithms can be used for strain analysis, particularly if a dense set of displacements within the deformation field can be distinguished, although they appear to be more computationally costly than the algorithm we use.

The work described in this paper uses micrographs of unpainted surfaces so that the flow patterns can be compared with features of the material. We apply a suitable optical flow method to a couple of particular instances that are considered to be of importance in materials science today. The chosen problems are very different, and have been selected to demonstrate an optical flow technique on different materials where inhomogeneous straining is expected. In both examples the material is well-known although the deformation process itself requires further understanding.

The first case observes the tensile properties of a heat-treatable aluminium alloy (Al 2024), both with and without laser welding. Al 2024 is commonly used in the aircraft industry. Weldments have heterogeneous properties both in the fused metal and in the surrounding heat affected zone; hence there will be significant strain gradients when they are tension loaded.

The second case is kink-band formation in a unidirectional carbon fibre composite. The compressive strength of such composites is generally just over half their tensile strength and the most common method of failure in compression is by fibre kinking. The understanding of kinking mechanisms and the prediction of critical kinking stress have been advanced markedly through the past three decades. However the mechanism of initiation and propagation of the kink bands is still not firmly established and little work has been done observing the dynamics of formation.

2 Image Analysis

A 768x576 pixel CCD camera is fitted to a Zeiss Axiolab microscope with a computer controlled moveable stage. A mechanical testing rig with a maximum load of 2 kN is fitted to the stage. The moveable stage is used to construct composite images of the whole surface as large as 3177x1060 pixels. The testing rig has also been fitted into the chamber of a scanning electron microscope equipped with a 1024x768 pixel CCD camera.

We use a new optical flow algorithm developed for image sequences exhibiting short-range and long range displacements, non-rigid deformations, and sensitivity to motion boundaries [7]. For each of a regularly spaced grid of points *(x,y)* a circular patch (radius 16 pixels) is defined in the same place on a pair of images I_1 and I_2. For each possible combination of pairs of pixels (one from each image patch) it is necessary to estimate the probability of the event that the two pixels represent a displacement by *(u,v)* between the image frames. The displacement probability for pixel grey values p_1 and p_2 is estimated by $\exp(-k(p_1-p_2)^2)$; this can be interpreted as a generalisation of the conservation of intensity assumption [9]. Therefore the displacement probability distribution function is estimated by accumulating the probabilities of every possible displacement within the patch:

$$P[u,v] = A[u,v] \sum_{\forall \left\{ \begin{matrix} x\text{-}x' = u; \\ y\text{-}y' = v \end{matrix} \right\}} \exp\left(\frac{(I_1[x,y] - I_2[x',y'])^2}{-\alpha} \right)$$

where *I(x,y)* is the intensity of the pixel at the position *(x,y)*, *A*[*u*,*v*] is a normalisation function reflecting the prior distribution of displacements within the patch, and α is a measure of the variance of greyscale values within the patch. The measured displacement for the optical flow vector is taken to be the value of (*u*,*v*) giving the maximum likelihood in *P*[*u*,*v*]. Function *P* is computed for every patch at the centre of which an optical flow vector is required. We use a patch size of radius 16 pixels, as the data demonstrates displacements of as much as 20 pixels between images. Because the distribution *P* is multimodal, the resulting flow field shows accurate estimation near motion contrast borders, and because all displacements within the patch are considered, estimation of non-rigid displacements is possible. Details are given in Clocksin [7], and an evaluation of this method in comparison with other standard optical flow algorithms has been carried out by Chivers [4].

The average strain is found over an area by fitting a strain tensor to the optical flow field. After Nye [12], the situation is modelled as the deformation of an extendible plane sheet. Let the point P, whose coordinates refer to axes fixed in space are (*x*,*y*) before deformation, move to P', with coordinates (*x*+*u*, *y*+*v*). A quantity known as the engineering strain tensor at point P' is defined as

$$e_{ij} = \begin{bmatrix} e_{11} & e_{12} \\ e_{21} & e_{22} \end{bmatrix} = \begin{bmatrix} \frac{\partial u}{\partial x} & \frac{\partial u}{\partial y} \\ \frac{\partial v}{\partial x} & \frac{\partial v}{\partial y} \end{bmatrix}.$$

It is necessary to estimate this tensor given the flow field. Data are obtained in the form of a set of *n* optical flow vectors $\vec{f}_i = (x_i, y_i, u_i, v_i)$ for i = 0, 1, …, *n*-1. With each data vector is associated an estimate σ_i^2 of the variance of the *P* distribution. The aim is to estimate a strain model having the least squared error fit to the data. The model

can be expressed as $M = \left\langle \begin{bmatrix} e_{11} & e_{12} \\ e_{21} & e_{22} \end{bmatrix}, \begin{bmatrix} o_x \\ o_y \end{bmatrix} \right\rangle$ where $\begin{bmatrix} e_{11} & e_{12} \\ e_{21} & e_{22} \end{bmatrix}$ is the engineering strain tensor and $\begin{bmatrix} o_x \\ o_y \end{bmatrix}$ defines the origin of the strain model. To perform a least-squares fit of the model M to the flow data $\vec{f}$, the problem is decomposed into two sub-problems:

1. Minimise $\chi^2 = \sum_{i=0}^{n-1} \left[\frac{u_i - (e_{11}x_i + e_{12}y_i + a)}{\sigma_i} \right]^2$ over parameters e_{11}, e_{12}, a;
2. Minimise $\chi^2 = \sum_{i=0}^{n-1} \left[\frac{v_i - (e_{21}x_i + e_{22}y_i + b)}{\sigma_i} \right]^2$ over parameters e_{21}, e_{22}, b.

Equating derivatives to zero, and rewriting in the form **Ax** = **b**, we have the two matrix equations:

$$\begin{bmatrix} \Sigma\frac{x_i^2}{\sigma_i^2} & \Sigma\frac{x_i y_i}{\sigma_i^2} & \Sigma\frac{x_i}{\sigma_i^2} \\ \Sigma\frac{x_i y_i}{\sigma_i^2} & \Sigma\frac{y^2}{\sigma_i^2} & \Sigma\frac{y_i}{\sigma_i^2} \\ \Sigma\frac{x_i}{\sigma_i^2} & \Sigma\frac{y_i}{\sigma_i^2} & \Sigma\frac{1}{\sigma_i^2} \end{bmatrix} \begin{bmatrix} e_{11} \\ e_{12} \\ a \end{bmatrix} = \begin{bmatrix} \Sigma\frac{x_i u_i}{\sigma_i^2} \\ \Sigma\frac{y_i u_i}{\sigma_i^2} \\ \Sigma\frac{u_i}{\sigma_i^2} \end{bmatrix} \text{ and } \begin{bmatrix} \Sigma\frac{x^2}{\sigma_i^2} & \Sigma\frac{x_i y_i}{\sigma_i^2} & \Sigma\frac{x_i}{\sigma_i^2} \\ \Sigma\frac{x_i y_i}{\sigma_i^2} & \Sigma\frac{y^2}{\sigma_i^2} & \Sigma\frac{y_i}{\sigma_i^2} \\ \Sigma\frac{x_i}{\sigma_i^2} & \Sigma\frac{y_i}{\sigma_i^2} & \Sigma\frac{1}{\sigma_i^2} \end{bmatrix} \begin{bmatrix} e_{21} \\ e_{22} \\ b \end{bmatrix} = \begin{bmatrix} \Sigma\frac{x_i v_i}{\sigma_i^2} \\ \Sigma\frac{y_i v_i}{\sigma_i^2} \\ \Sigma\frac{v_i}{\sigma_i^2} \end{bmatrix}.$$

With the **A** and **b** matrices obtained from the set of flow vectors, **x** may be found by standard methods.

Given a strain model *M*, it is possible to synthesise an 'ideal' flow field that depicts the model. Express an ideal flow vector as $\tilde{f}_i = (\tilde{x}_i, \tilde{y}_i, \tilde{u}_i, \tilde{v}_i)$ where the components are obtained from

$$\begin{bmatrix} \tilde{u}_i \\ \tilde{v}_i \end{bmatrix} = \begin{bmatrix} e_{11} & e_{12} \\ e_{21} & e_{22} \end{bmatrix} \begin{bmatrix} \tilde{x}_i - o_x \\ \tilde{y}_i - o_y \end{bmatrix} = \begin{bmatrix} e_{11} & e_{12} \\ e_{21} & e_{22} \end{bmatrix} \begin{bmatrix} \tilde{x}_i \\ \tilde{y}_i \end{bmatrix} + \begin{bmatrix} a \\ b \end{bmatrix} = \begin{bmatrix} e_{11} & e_{12} & a \\ e_{21} & e_{22} & b \end{bmatrix} \begin{bmatrix} \tilde{x}_i \\ \tilde{y}_i \\ 1 \end{bmatrix}.$$

where $a = -(e_{11}o_x + e_{12}o_y)$ and $b = -(e_{21}o_x + e_{22}o_y)$.

3 Aluminium Alloy in Tension

The aluminium alloy (2024-T3) was tested in tension using unwelded 'dogbone' samples (gauge width ~2mm; gauge length ~5mm), and using cross-section samples (thickness ~1.5mm) cut across a laser weld. Both unwelded and welded samples were cut from 1.6mm sheet. Prior to testing, the samples were polished and (for the optical work) anodised to reveal the grain structure. Loading was at a strain rate of $6\text{x}10^{-5}$ and the straining was paused whilst images were acquired. In what follows, the

metallurgical details have been suppressed in the interests of an image processing readership, but are available from [5].

3.1 Unwelded Samples

Figure 1 shows a pair of images from straining sequence; each image shows a region about 2mm across. Figure 2 shows the resulting optical flow field showing the pattern of material deformation. Any optical flow field will be affected by missing, ambiguous or noisy data, and the figure shows a number of places where flow vectors are not available. Figure 2b shows a synthetic flow field generated by estimating the strain tensor of the data field in Figure 2a. Here a classic surface strain pattern can be seen.

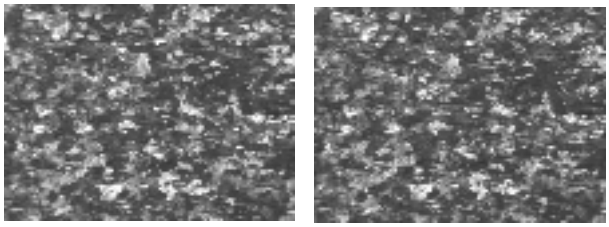

Figure 1. A pair of images taken a few seconds apart during the application of axial tensile force.

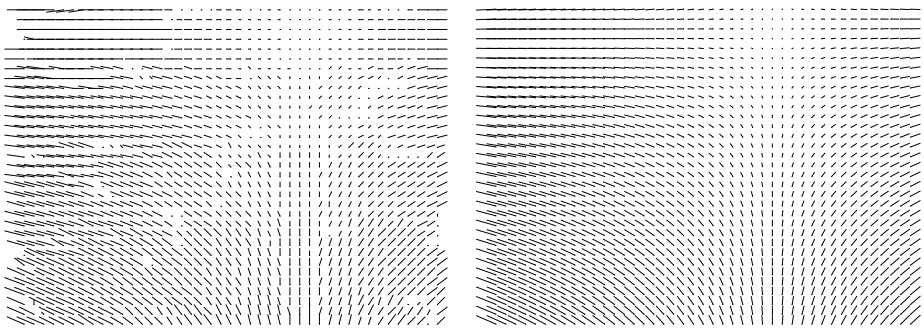

Figure 2 (a) Flow field calculated from the image pair in Figure 1. (b) 'Ideal' flow field synthesised from the strain tensor estimated from flow vectors in (a).

In the subsequent flow maps, only the raw flow field will be shown. While the synthesised flow map has a certain appeal, it can disguise phenomena of metallurgical significance such as discontinuities by oversmoothing the data.

Figure 3 shows the opening of a crack across precipitates in unwelded material viewed through a scanning electron microscope. The flow field for the whole image seems relatively smooth, but when the flow is measured at a slightly higher resolution (Figure 4), discontinuous motion can be seen about the cracks (labelled BC in Figure 4b). Lines of high strain representing local shear and rotation can be seen at approximately 45° from the both ends of the crack, particularly in the direction between the two cracks (AB).

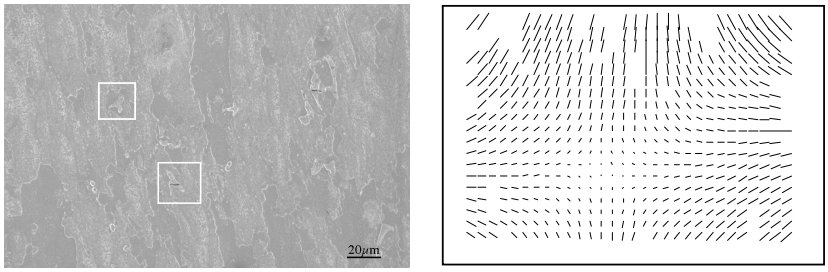

(a) (b)

Figure 3 (a) One image within the sequence of SEM images (at x500 magnification) of Al 2024 tensile test specimen (thickness is 1.1 mm) with vertical axis of loading at 413 MPa. The white boxes and the scale bar have been superimposed; the white boxes surround precipitates, and are not relevant in this context. (b) The flow field calculated for a pair of images (the image in (a) and one taken at 445 MPa).

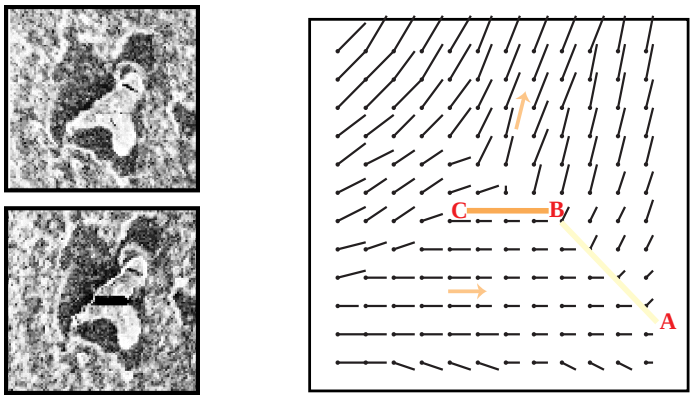

(a) (b)

Figure 4. (a) A pair of images showing cracked precipitates of Cu-rich phase. (b) Optical flow around these precipitates showing local shear and rotation.

3.2 Welded Samples

Here a cross-section sample of Al 2024-T3 of thickness ~1.5mm was cut across a laser weld. The welds deform differently from the unwelded aluminium, owing to the variation in yield stress and ductility with position, and because of the presence of cracks, pores and other defects. The weld bead provides an asymmetry to the cross-section (about the loading direction), which results in a strain gradient across the width of the sample. Figure 5a shows one of the images used, and Figure 5b,c shows two optical flow maps relating to strain intervals in early and late stages of deformation.

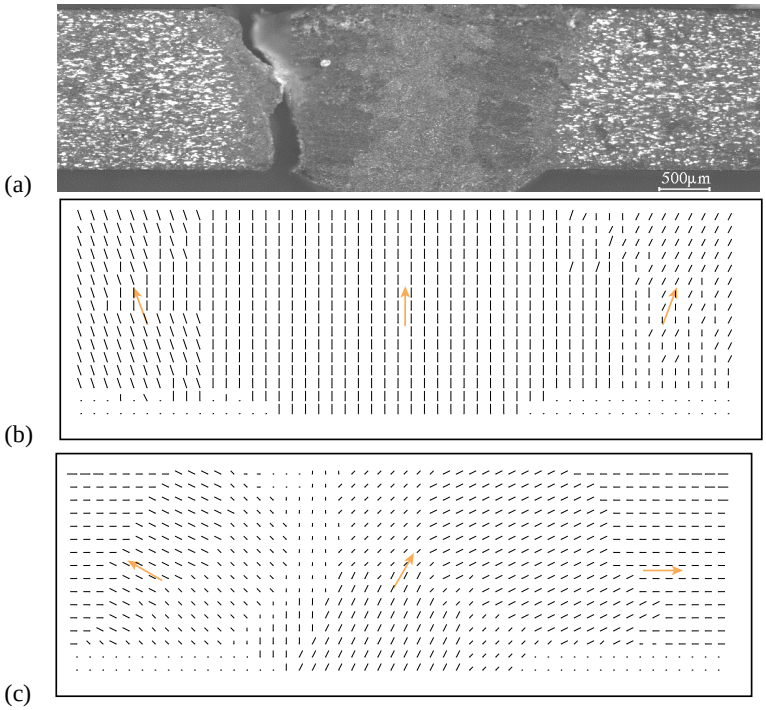

Figure 5. (a) Image of weld; the bead occupies the central 1/3 of the image. (b) Flow map in early stage of deformation; (c) Flow map in late stage of deformation. Grey arrows are overlaid to illustrate deformations.

From the beginning of plasticity, the deformation starts to become concentrated in the (softer) weld metal. The stress-reducing effect of the bead geometry causes the localisation to be off-centre, near the edge of the weld, where the sample will finally fracture. Before macroscopic failure, there is some growth of small cracks in this area, providing a high local strain.

4 Carbon Fibre Kinking

The carbon fibre (T300)/epoxy (914) composite samples (cross section ~1.6 x 2.2 mm; gauge length ~5 mm) were compressed by mixed end and shear loading. The fibres were aligned at 10°, 15° and 20° to the axis of loading. Loading was at a strain rate of $6x10^{-5}$ and the straining was paused whilst images were acquired.

The sample shown in Figure 6 was cut at 20° to the fibre direction and failed by the gradual formation of a kink band. Compression occurs at an almost constant load after the initial maximum stress. Off-axis compression can be explained by the increased ease of interlaminar sliding due to matrix plasticity.

Interestingly, in the carbon-fibre studies the flow fields show significant evidence of shear in the position of the kink band *before* the maximum stress is reached (for example Figure 7b,c) or any 'kinking' is visible to the eye. The strain is greatest at the bottom of this band near to the corner of the constraint plate. This is in keeping with the concept that the kink band might nucleate at the free surface. Spowart and Clyne [14] also presented some evidence for such an effect, although they were not able to

view the developing strain field directly. However, it should be noted that the nucleation point was consistently observed as being close to the grips, so it is possible that grip constraint was having an influence on the kink-band nucleation process.

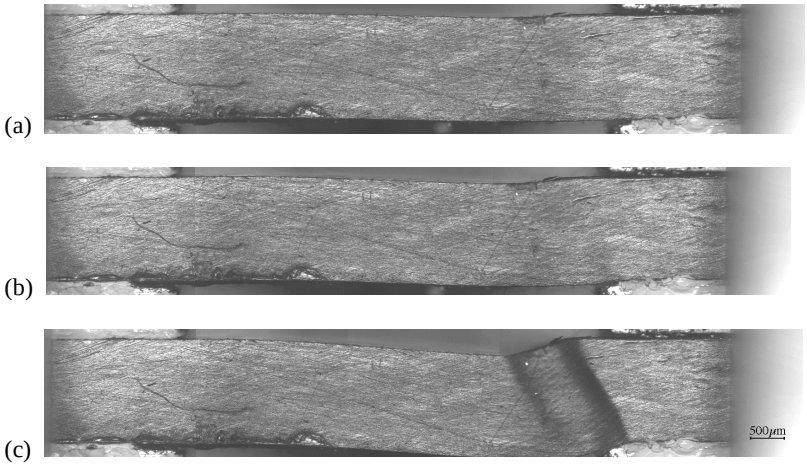

Figure 6. Carbon fibre sample. (a) Sample imaged just before maximum load; (b) just after maximum load; (c) after the kink band has properly developed.

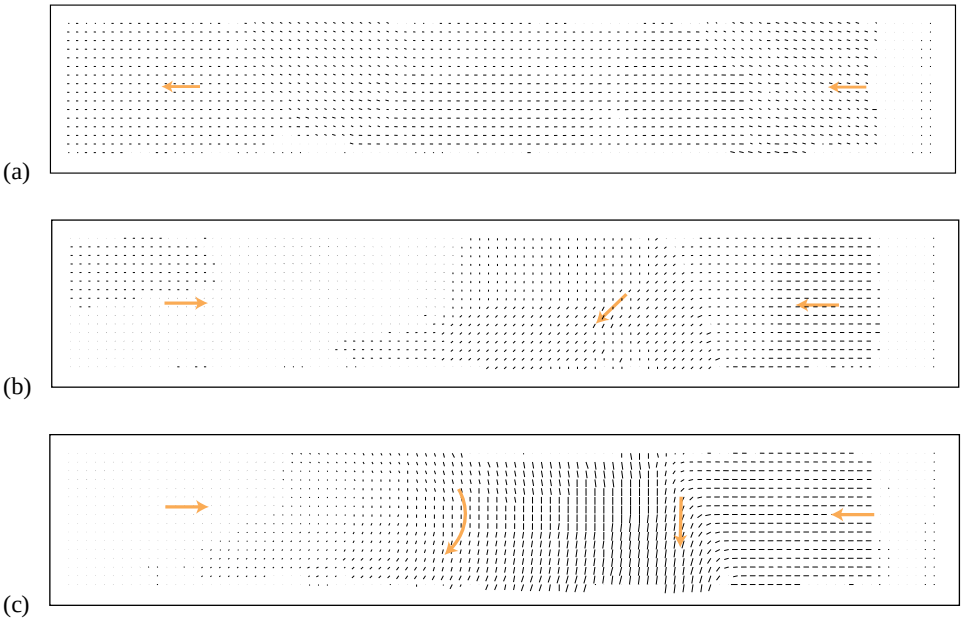

Figure 7. Flow fields found during carbon-fibre test. (a) Axial strain similar to Figure 2; (b) Shear beginning at right-hand grip; (c) Showing larger scale shear and rotation as the stress maximum is passed.

Samples with 10° and with 15° off-axis fibre direction failed by the rapid formation of a kink-band (Figure 8). From examination of flow fields from images taken at regular intervals during testing, the kinking process appears to be similar for both angles. The flow prior to kinking varied from sample to sample, but there were some commonly occurring patterns. Immediately prior to kinking, there was often shear in the area in which the kink band was to form and resulting rotation of the main part of the sample.

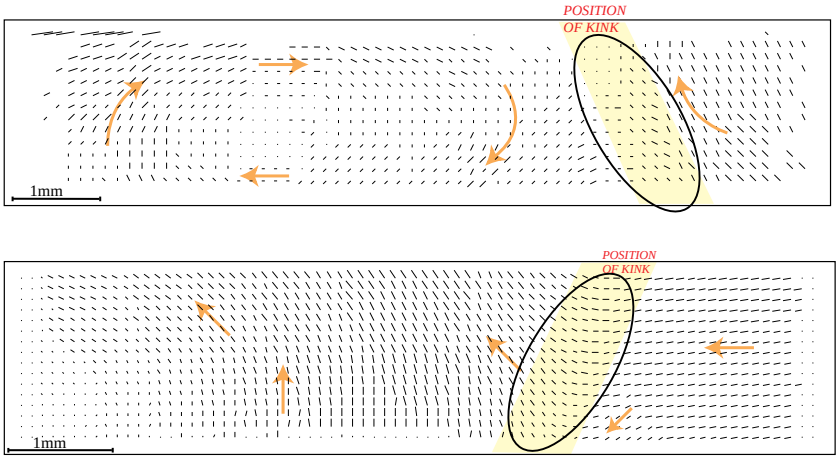

Figure 8. Samples with (a) 10° and (b) 15° off-axis fibre direction, showing rotation and shear prior to kinking. The overlaid grey arrows illustrate deformations, and the overlaid ellipse shows the position of the kink when it develops.

5 Conclusions

The optical flow algorithm works well for anodised but otherwise untreated aluminium samples, and particularly well for the carbon fibre composite materials, providing comprehensive and self-consistent flow fields. In both the aluminium and composite materials, the optical flow maps revealed significant features prior to macroscopic material failure. Because the algorithm is accurate at motion contrast borders, strain maps are available at regions of high change of strain and for inhomogeneous deformations. This suggests the possible application of suitable optical flow algorithms to the in-situ inspection of materials. Such inspection has been carried out at several different scales, demonstrating the versatility of the optical flow method by contrast to mechanical or interferometric methods.

Smooth flow maps may also be obtained by fitting a strain tensor to the raw flow vectors, then synthesising the ideal flow map given the strain tensor. This gives a way of representing flow fields in general using only six parameters (the four-element strain tensor and the two-element origin), and could provide a novel method for determining optical flow using an underlying assumption of plastic strain, particularly where relatively smooth fields are expected and where suboptimal viewing conditions provide sparse or noisy flow maps.

Acknowledgements

This work was supported by EPSRC grant GR/M29177 to Professor Phil Withers and Dr Clocksin. Miss Chivers was supported by an EPSRC CASE postgraduate studentship. We thank Professor Withers of Manchester University, Professor Bill Clyne of the DERA Gordon Laboratory Cambridge, and Professor Ron McEwen of British Aerospace for much valuable advice. We also are indebted to Dr Stuart Hill and Miss Shivani Agarwal for discussions and technical assistance.

References

1. Barron, J.L, D.J. Fleet and S.S. Beauchemin, 1994. Performance of optical flow techniques. *International Journal of Computer Vision* **12**(1), 43-77.
2. Beauchemin, S.S. and J.L. Barron, 1995. Computation of optical flow. *ACM Computing Surveys* **27**(3), 433-467.
3. Burch, J.M., 1974. Holographic measurement of displacement and strain – an introduction. *Journal of Strain Analysis* **9**(1), 1-3.
4. Chivers, K.F., 1997. Surface strain mapping of heterogeneous materials. CPGS Report, Department of Materials Science and Metallurgy, University of Cambridge.
5. Chivers, K.F., 2000. Observations of surface strain in heterogeneous materials across a range of scales using optical flow, forthcoming PhD dissertation, Department of Materials Science and Metallurgy, University of Cambridge.
6. Chu, T.C, W.F. Ranson, M.A. Sutton and W.H. Peters, 1985. Applications of digital image correlation techniques to experimental mechanics. *Experimental Mechanics* **25**(3), 232-244.
7. Clocksin, W.F., 1997. A new method for estimating optical flow. Technical Report 436, Computer Laboratory, University of Cambridge.
8. Hayton, P.M., Brady, M., Smith, S.M. and Moore, N., 1999. A non-rigid registration algorithm for dynamic breast MR images. *Artificial Intelligence* **114**, 125-156.
9. Horn, B.K.P. and B.G. Schunck, 1981. Determining optical flow. *Artificial Intelligence* **17**, 185-204.
10. Kuang, J.H. and L.S. Chen, 1995. A single strain-gauge method for K-1 measurement. *Engineering Fracture Mechanics* **51**(5), 871-878.
11. Lehman, F., undated. Local deformation field measurement using digital speckle photography. Technical Report, Instron Corp., Canton, MA 02021, USA.
12. Nye, J.F., 1957. *Physical properties of crystals: their representation by tensors and matrices*. Oxford University Press.
13. Simoncelli, E.P., E.H. Adelson and D.J. Heeger., 1991. Probability distributions of optical flow. *Proc. IEEE Conference on Computer Vision and Pattern Recognition*, Mauii. 310-315.
14. Spowart, J.E. and T.W. Clyne, 1999. The axial compressive failure of titanium reinforced with silicon carbide monofilaments. *Acta Materialia* **47**(2), 671-687.
15. Yoshida, S., R. Suprapedi, M. Widiastuti, M. Pardede, S. Huagalong, J.S. Marpaung, A.F. Murhardy and A. Kusnowo, 1996. Direct observation of developed plastic deformation and its application to non-destructive testing. *Japanese Journal of Applied Physics* **35**(7A), L854-L857.
16. Zhang, D., Zhang, X., and G. Cheng, 1999. Compression strain measurement by digital speckle correlation. *Experimental Mechanics* **39**(1), 62-65.